



Integrating noble-metal-free metallic vanadium carbide cocatalyst with CdS for efficient visible-light-driven photocatalytic H₂ evolution

Lei Tian^{a,b,c}, Shixiong Min^{a,b,c,*}, Fang Wang^{a,b,c}



^a School of Chemistry and Chemical Engineering, Key Laboratory of Electrochemical Energy Conversion Technology and Application, North Minzu University, Yinchuan, 750021, PR China

^b Key Laboratory of Chemical Engineering and Technology, State Ethnic Affairs Commission, North Minzu University, Yinchuan, 750021, PR China

^c Ningxia Key Laboratory of Solar Chemical Conversion Technology, North Minzu University, Yinchuan, 750021, PR China

ARTICLE INFO

Keywords:

Vanadium carbide
Cocatalyst
CdS
Photocatalytic H₂ evolution
Visible light

ABSTRACT

Developing highly active and stable cocatalysts at lower costs is greatly crucial for high-performance semiconductor-based photocatalytic H₂ evolution from water splitting. Herein, we report that noble-metal-free metallic vanadium carbide (VC) can function as a superior cocatalyst when integrated with CdS for efficient photocatalytic H₂ evolution under visible light irradiation (≥ 420 nm). The most efficient CdS/VC (15 wt.%) composite photocatalyst exhibits an exceptionally high photocatalytic H₂ evolution rate of $14.2 \text{ mmol H}^{-1} \text{ g}^{-1}$, up to 12 times higher than that of pristine CdS. The apparent quantum efficiency (AQE) of H₂ evolution reaches up to 8.7% at 420 nm. Moreover, the CdS/VC (15 wt.%) shows good stability for H₂ evolution after eight consecutive cycles of continuous light irradiation of 40 h. Most notably, the H₂ evolution activity of CdS/VC is even higher than or comparable to that of platinized CdS (CdS/Pt) prepared by photoreduction or chemical reduction at the same cocatalyst loading (1 wt.%). Furthermore, VC can also serve as an efficient H₂ evolution cocatalyst on various semiconductor photocatalysts (TiO₂ and g-C₃N₄) and in a dye-sensitized photocatalytic system. Electrochemical and photoelectrochemical measurements reveal that VC can function as an efficient electrocatalyst not only to reduce the overpotential of H⁺/H₂O reduction to H₂ but also to effectively capture the photogenerated electrons of CdS for enhancing the separation efficiency of photogenerated carriers thanks to its outstanding metallic conduction, thus substantially improving the photocatalytic H₂ evolution activity of CdS/VC photocatalyst. This work demonstrates that noble-metal-free VC is a promising alternative to Pt as an efficient H₂ evolution catalyst for electrocatalytic and photocatalytic energy conversion.

1. Introduction

Hydrogen (H₂) production via light-driven photocatalytic water splitting reaction on semiconductor photocatalysts is a promising technology to reduce the ever-increasing global energy crisis and environmental pollution [1–3]. To make the conversion of solar energy into hydrogen energy efficiently, a semiconductor photocatalyst that has a suitable band gap for visible light absorption, sufficient reductive potential of the conduction band (CB) electrons for H⁺/H₂O reduction, and long-term stability is highly required [4–7]. Up to date, a number of ultraviolet- and visible-light-responsive semiconductor photocatalysts have been developed for photocatalytic H₂ evolution reaction (HER) [8–12]. Among them, visible-light-responsive CdS with a band gap of *ca.* 2.4 eV is one of the most prominent photocatalysts for photocatalytic HER because of its high visible light harvesting capacity (that

can absorb light with a wavelength lower than 520 nm), good charge carrier mobility, and suitable band edge potentials [13–16]. However, the H₂ evolution activity and stability of pristine CdS is still low due to the fast recombination of photogenerated electrons and holes, high energy barrier at surface sites for H₂ evolution, and intrinsic photo-corrosion [17–19]. It has been well-recognized that loading a H₂ evolution cocatalyst (HEC) onto the surfaces of CdS cannot only effectively promote the separation of photoexcited electrons and holes but also greatly lower the kinetic barrier of HER [20–23]. At present, the most efficient HEC are mainly noble metals and their oxides (Pt, RuO₂, IrO₂, etc.); however, their large-scale application in photocatalytic HER has been largely hampered because of their low abundance and thus high cost [24–27]. Therefore, developing highly active cocatalysts based on earth-abundant materials has been intensely pursued aiming to improve the photocatalytic H₂ evolution performance of CdS under visible light

* Corresponding author at: School of Chemistry and Chemical Engineering, Key Laboratory of Electrochemical Energy Conversion Technology and Application, North Minzu University, Yinchuan, 750021, PR China.

E-mail address: sxmin@nun.edu.cn (S. Min).

irradiation.

Recently, several transition-metal-based cocatalysts at lower costs including oxides [28], hydroxides [29], sulfides [30], selenides [31], nitrides [32], and carbides [33], have been identified as the promising alternatives to noble-metal-based cocatalysts for improving photocatalytic H₂ evolution efficiency. Particularly, Pt-like transition metal carbides (TMCs) (e.g., Mo₂C, Ti₃C₂ MXene, and Ni₃C) [34–37] have been recently identified as the efficient HECs in photocatalytic HER, since these TMCs with high conductivity not only favors the fast electron transport but also provides Pt-like active sites for H₂ evolution. In fact, it has been reported that Ni₃C and Ti₃C₂ MXene have shown to act as the highly active cocatalysts of CdS for efficient photocatalytic HER under visible light irradiation [36,37]. Mo₂C cocatalyst has also been embedded into the g-C₃N₄ matrix for enhanced visible-light-driven H₂ evolution [35,38]. Most recently, a number of vanadium-based catalysts, such as VS₂ nanosheets and VC, have been found to exhibit superior activity for electrocatalytic HER [7,39]. Notably, as a newly emerging TMC, VC has been used as an efficient catalyst due to its high activity, selectivity, stability, and resistance to poisoning. In addition, density functional theory (DFT) calculations have predicted that VC possesses metallic properties with lower electrical resistivity comparable to Mo₂C and similar H binding energy (ΔG_H^{*}) to Mo₂C and WC. More importantly, compared to Mo₂C and WC, VC has smaller density that could offer a larger exposed surface area [2,39], thus it could be anticipated that VC will be a promising HEC material that can be employed in photocatalytic HER. However, to the best of our knowledge, there is no report on employing VC as a cocatalyst for promoting photocatalytic H₂ evolution over CdS under visible light irradiation.

In this work, we explore the potential of noble-metal-free VC as a HEC of CdS photocatalyst for efficient photocatalytic H₂ evolution under visible light irradiation (≥ 420 nm). The VC can be facilely integrated with CdS by a simple solution-based mixing method, leading to CdS/VC composite photocatalysts with tunable composition. The most efficient CdS/VC (15 wt.%) photocatalyst exhibits a superior photocatalytic H₂ evolution activity, which is 12 times higher than pristine CdS. More importantly, CdS/VC even demonstrates a higher photocatalytic activity for H₂ evolution than Pt loaded CdS (CdS/Pt-P) prepared by in situ photoreduction method and comparable to CdS/Pt-B prepared by chemical reduction method using NaBH₄ as reductant. The cocatalyst role of VC and the origin of the high photocatalytic H₂ evolution activity of integrated CdS/VC photocatalyst are investigated by electrochemical, photoelectrochemical, and spectroscopic techniques. Moreover, the versatility of VC as a highly active cocatalyst for other semiconductor photocatalysts (TiO₂ and g-C₃N₄) and dye-sensitized system is also confirmed, demonstrating the huge potential of inexpensive VC as a promising HEC to replace rare and costly Pt for designing high-performance photocatalysts for large-scale light-induced photochemical energy conversion.

2. Experimental section

2.1. Chemicals and materials

All chemicals were of analytical grade and used as received without further purification. VC nanoparticles were purchased from Hefei Zhonghang Nanometer Technology Development Co., Ltd., TiO₂ nanoparticles (P25, 20% rutile and 80% anatase) were purchased from Degussa, V₂O₅ was obtained from Beijing Chemical Works, H₂PtCl₆ and AgNO₃ were obtained from Tianjin Guangfu Fine Chemical Research Institute, triethanolamine (TEOA, 99.8%) was purchased from Xilong scientific, and Erythrosin B (ErB) was obtained from Tianjin Guangfu Fine Chemical Research Institute. All solutions in the experiments were prepared with ultrapure water (> 15 MΩ) that was obtained by an YL-100B-D water-purification system. g-C₃N₄ nanosheets were prepared by pyrolyzing urea at 550 °C for 2 h according to a reported procedure [8].

2.2. Preparation of CdS/VC composite photocatalysts

Well-crystallized CdS nanoparticles were synthesized according to a reported procedure [40]. Briefly, an aqueous solution of 0.14 M Na₂S (800 mL) was added slowly to 0.14 M Cd(CH₃COO)₂ solution (1000 mL) under vigorous stirring. The obtained yellow slurry mixture was stirred for 24 h and kept for an additional 24 h. The resulting yellow slurry was filtered. The wet solid was suspended in pure water (120 mL) and transferred to two Teflon-lined autoclaves (100 mL) and heated at 200 °C for 72 h. The yellow solid was filtered, washed with water several times, and dried under vacuum at 60 °C for 24 h.

CdS/VC composite photocatalysts were prepared by a facile solution-based mixing method. In a typical synthesis procedure, 1.0 g of CdS nanoparticles was dispersed into 200 mL of water containing different amounts of VC by ultrasonication, and the resultant mixture was stirred at room temperature for 0.5 h to form a homogeneous suspension. After that, the suspension was collected by filtration with a 0.22 μm microporous membrane, and then dried in a vacuum oven at 60 °C for 24 h. The weight ratios of VC to CdS were controlled to be 0 wt.%, 0.5 wt.%, 1 wt.%, 5 wt.%, 10 wt.%, 15 wt.%, 20 wt.%, 25 wt.%, and 30 wt.%. For the purpose of comparison, CdS nanoparticles and VC were also treated under the same experimental conditions for preparation of CdS/VC composite photocatalysts.

VC was also integrated, respectively, with TiO₂ and g-C₃N₄ by the identical preparation processes for CdS/VC to prepare TiO₂/VC (15 wt.%) and g-C₃N₄/VC (15 wt.%) photocatalysts. Furthermore, VC was also integrated with a Erythrosin B-triethanolamine (ErB-TEOA) dye-sensitized system.

In addition, 15 wt.% V₂O₅ was also integrated with CdS (CdS/V₂O₅ (15 wt.%) by the exact same procedures for preparation of CdS/VC (15 wt.%). 1 wt.% Pt and Ag were, respectively, loaded on CdS by the in situ photoreduction from the corresponding complexes of metals, and the resultant samples were denoted as CdS/Pt-P (1 wt.%) and CdS/Ag-P (1 wt.%), respectively. Furthermore, 1 wt.% Pt loaded CdS photocatalyst (denoted as CdS/Pt-B (1 wt.%) was also prepared with chemical reduction method using NaBH₄ as reductant [41].

2.3. Characterization

Transmission electron microscopy (TEM) and high-resolution TEM (HRTEM) images were taken with a Tecnai-G²-F30 field emission transmission electron microscope. X-ray diffraction (XRD) patterns were obtained with a Rigaku smartlab diffractometer with a nickel filtrated Cu K α radiation. X-ray photoelectron spectroscopy (XPS) was performed on an X-ray photoelectron spectrometer (Thermo Scientific Escalab-250Xi) equipped with a monochromatic Al K α X-ray source. UV-vis diffuse reflectance spectra were recorded on a PerkinElmer Lambda-750 UV-vis-near-IR spectrometer equipped with an integrating sphere and BaSO₄ powders were used as a reflectance standard. Photoluminescence spectra were determined by a Horiba Scientific FluoroMax-4 spectrofluorometer spectrometer. The fluorescence decay times were measured using the Horiba Jobin Yvon Data Station HUB operating in time correlated single photon counting mode (TCSPC) with the time resolution of 200 ps. Nano LED diode emitting pulses at 370 nm with 1 MHz repetition rate was used as an excitation source. Light-scattering Ludox solution was used to obtain the instrument response function (prompt). The time ranges are 0.055 ns/channel in 4096 effective channels. Horiba Jobin Yvon DAS6 fluorescence decay analysis software was used to fit the model functions to the experimental data.

2.4. Photocatalytic H₂ evolution experiments

The photocatalytic H₂ evolution experiments were performed in a 250 mL reaction cell connected to a closed gas circulation and evacuation system (CEL-SPH2N, CEAULIGHT). A 300-W Xe lamp (CEL-

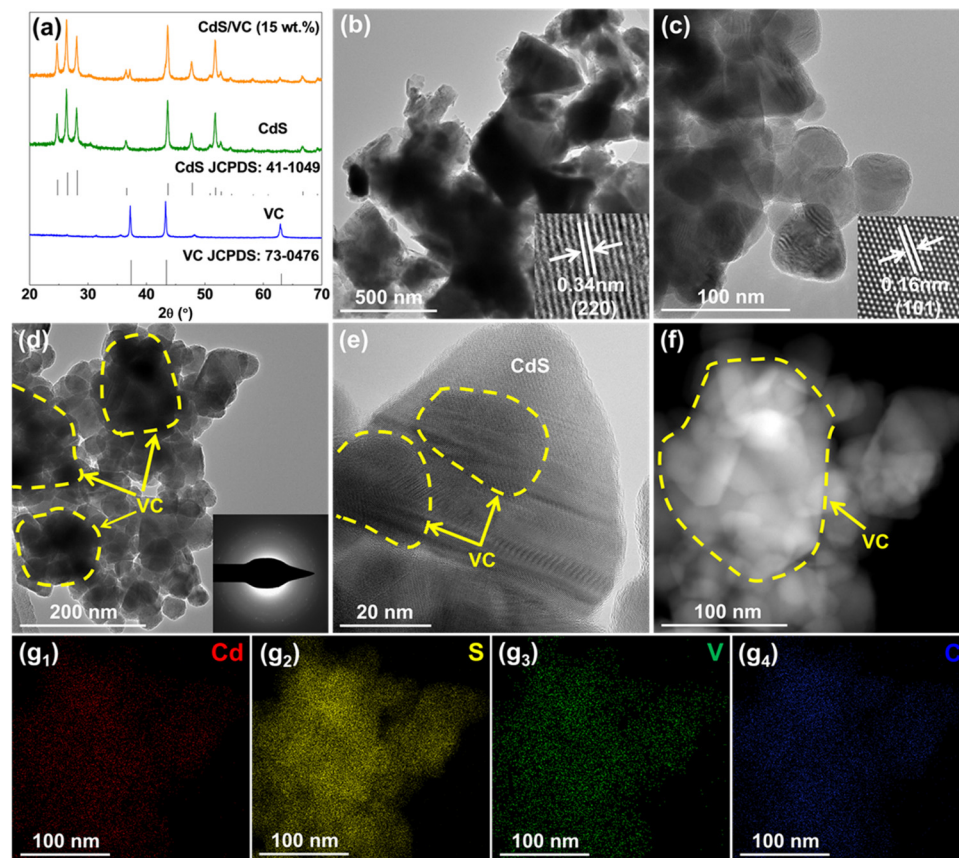


Fig. 1. (a) XRD patterns of pristine CdS, commercial VC, and CdS/VC (15 wt.%). (b–d) TEM images of (b) commercial VC, (c) pristine CdS, and (d) CdS/VC (15 wt.%). The insets in panel (b) and (c) show the HRTEM images of (b) commercial VC and (c) pristine CdS, respectively. The inset in panel (d) shows the corresponding SAED pattern of CdS/VC (15 wt.%). (e) HRTEM image of CdS/VC (15 wt.%). (f) HAADF-STEM image of CdS/VC (15 wt.%) and (g) corresponding elemental mappings (Cd, S, V and C).

HXF300) equipped with an optical cut-off filter ($\lambda \geq 420$ nm) was used as light source. In a typical experiment, 40.0 mg of the photocatalyst was dispersed into 100 mL of aqueous solution containing 10 vol.% lactic acid (LA, pH 1.2) as the sacrificial reagent by ultrasonication for 10 min. Before light irradiation, the reaction system was thoroughly degassed by evacuation in order to remove the oxygen inside the reactor and dissolved in solution. The reaction solution was continuously stirred and maintained at 6 °C by a flow of cooling anhydrous ethanol. The photocatalytic H₂ evolution experiments of TiO₂/VC (15 wt.%) and g-C₃N₄/VC (15 wt.%) were performed in 10 vol.% LA (pH 1.2) and 10 vol.% TEOA (pH 11), respectively, where a 300-W Xe lamp without a cutoff filter was used as light source with the main emission wavelength ranging from 320 to 800 nm (Fig. S1). For ErB-sensitized photocatalytic H₂ evolution experiment, 6 mg of VC was dispersed into 100 mL of 15 vol.% TEOA solution (pH 9) containing 34 mg of ErB under visible light irradiation (300-W Xe lamp with a 420 nm cut-off filter). The amount of evolved H₂ was determined using an on-line gas chromatograph (CEL-GC-7920, TCD, N₂ carrier).

The apparent quantum efficiency (AQE) of H₂ evolution was measured under conditions similar to those in the above photocatalytic reaction except that the light source was equipped with various band-pass filters (420, 475, 520, 550, 600 nm). The photon flux of incident light was determined using a Ray virtual radiation actinometer (Apogee MQ-500, silicon ray detector, light spectrum, 389–692 nm; measurement range, 0–4000 mol⁻¹ m⁻² s⁻¹). The AQE was calculated from the ratio of the number of reacted electrons during H₂ evolution to the number of incident photons according to Eq. (1) below:

$$\text{AQE}(\%) = \frac{2 \times \text{number of evolved H}_2 \text{ molecules}}{\text{number of incident photons}} \times 100 \quad (1)$$

2.5. Electrochemical and photoelectrochemical measurements

All the electrochemical and photoelectrochemical measurements were performed on an electrochemical workstation (CHI760E, Shanghai, China) in a three-electrode cell. A Pt mesh (1 cm × 1 cm) was used as the counter electrode, and a saturated Ag/AgCl electrode was used as the reference electrode. The working electrode was prepared by a spin-coating process. The homogenous photocatalyst suspension was prepared by dispersing 10 mg of photocatalyst powder into the mixture of ethanol (1 mL) and 1 wt.% Nafion-ethanol solution (1 mL) by ultrasonication. After that, 0.4 mL of photocatalyst suspension was spin-coated onto the conductive side of a ITO glass (2.5 cm × 2.5 cm) and the obtained electrode was dried in a flow of air and dried at 50 °C for 24 h. The geometrical surface area of working electrode exposed to the electrolyte was controlled to be 1.13 cm². To ensure a certain stability of the photoanodes, a mixed solution of 0.5 M Na₂SO₄ containing 10 vol.% LA was used as supporting electrolyte. Before the test, the solution was bubbled with N₂ (40 mL min⁻¹) for 10 min. The transient photocurrent response was recorded at a bias of 0.5 V vs. Ag/AgCl under chopped visible light irradiation. A 300-W Xe lamp equipped with a 420 nm cut-off filter was used as light source. Electrochemical impedance spectroscopy (EIS) was carried out at a forward bias of 0.5 V vs. Ag/AgCl with an AC amplitude of 5 mV in the frequency range of 10 mHz to 100 kHz under the visible light irradiation. The electrocatalytic H₂ evolution activity was measured using linear sweep voltammetry (LSV) with a scan rate of 5 mV s⁻¹. A graphite rod and a saturated Ag/AgCl electrode were used as the counter and reference electrodes, respectively. The photocatalysts were loaded onto the carbon paper (CP) to obtain the working electrodes as follows: the homogenous photocatalyst suspensions were prepared by dispersing CdS (11.3 mg), VC (2 mg), or CdS/VC (15 wt.%) (13.3 mg) powders into the mixed solution of 1 mL of ethanol-water (4/1, v/v) and 50 μL of 1 wt.% Nafion-ethanol solution by ultrasonication for 0.5 h. Then,

0.6 mL of photocatalyst suspensions were drop-coated onto the CP and the obtained electrodes were dried on the electric hot plate at 260 °C. The geometrical surface areas of working electrodes exposed to the electrolyte were controlled to be 0.5 cm².

3. Results and discussion

The crystalline structure of the as-prepared photocatalysts was examined using the X-ray diffraction (XRD). Fig. 1a shows the XRD patterns of pristine CdS, commercial VC, and CdS/VC (15 wt.%) composite photocatalyst. For the pristine CdS, a number of strong characteristic diffraction peaks were observed at 2θ values of 24.7°, 26.4°, 28.1°, 43.6°, 47.6°, and 51.7°, which can be indexed to the (100), (002), (101), (110), (103), and (112) crystal planes of the well-crystallized hexagonal CdS (JCPDS 41-1049), respectively [42,43]. The crystalline size of CdS nanoparticles was calculated to be *ca.* 30 nm. As to the commercial VC, the diffraction peaks at 2θ values of 37.4°, 43.4°, 63.1°, and 75.7° can be assigned to the (111), (200), (220), and (311) crystal planes of the cubic VC (JCPDS 73-0476), respectively [39]. After CdS being integrated with VC, both the characteristic diffraction peaks of CdS and VC are observed in the XRD pattern of the CdS/VC (15 wt.%) composite photocatalyst without any detectable impurities, suggesting the success integration of CdS and VC, and that the presence of VC has no influence on the crystalline structure of CdS [10,43] (Table 1). In addition, for the CdS/VC composite photocatalysts, the intensity of diffraction peaks ascribed to the hexagonal CdS tends to be weaker, whereas the diffraction peaks of the cubic VC become stronger with increasing VC content (Fig. S2). The effect of integration of VC on the physicochemical properties of the resultant CdS/VC composite photocatalysts such as the Brunauer-Emmett-Teller (BET) specific surface area (S_{BET}), the pore size distribution, and the pore structure were investigated by N₂ adsorption-desorption measurements at 77 K (Fig. S3), and the obtained results were summarized in Table 1. The N₂ isotherm of pristine CdS is identified as type IV isotherm with type H3 hysteresis loop with a S_{BET} of 31.0 m² g⁻¹, indicative of the presence of mesoporous structure, which is probably formed by the aggregations of CdS nanoparticles [10,43]. As to the commercial VC sample, it shows smaller S_{BET} of 6.8 m² g⁻¹, average pore size of 14.5 nm, and total pore volume of 0.024 cm³ g⁻¹ than pristine CdS. All the CdS/VC composite photocatalysts at lower VC contents exhibit similar N₂ isotherms and pore size distribution curves to pristine CdS, while the S_{BET} of CdS/VC composite photocatalysts will slightly decrease at higher VC contents due to the presence of low-surface-area VC, indicating that the integration of VC has a negligible effect on the physicochemical properties of the CdS and *vise versa* [4]. The variation of S_{BET} for CdS/VC photocatalysts does not play a crucial role in photocatalytic HER of CdS/VC composite photocatalysts [10], see detailed discussion below.

Table 1

Physicochemical properties of pristine CdS, commercial VC, and CdS/VC samples with different contents of VC.

Samples	S_{BET} (m ² g ⁻¹) ^a	Average pore size (nm) ^b	Total pore volume (cm ³ g ⁻¹) ^c	Crystallite size (nm) ^d
Pristine CdS	31.0	36.5	0.283	29.2
CdS/VC (0.5 wt.%)	30.6	36.8	0.281	28.9
CdS/VC (1 wt.%)	32.7	37.6	0.308	28.8
CdS/VC (5 wt.%)	28.9	35.3	0.255	28.0
CdS/VC (10 wt.%)	28.5	35.2	0.251	28.0
CdS/VC (15 wt.%)	30.0	39.8	0.299	26.9
CdS/VC (20 wt.%)	23.4	33.4	0.195	29.8
CdS/VC (25 wt.%)	27.9	33.1	0.231	29.0
CdS/VC (30 wt.%)	21.5	37.2	0.200	29.0
Pristine VC	6.8	14.5	0.024	36.9

^a BET surface area is calculated from the linear part of the BET plot.

^b Adsorption average pore width (4 V/A by BET).

^c Single point total pore volume of the pores at $P/P_0 = 0.99$.

^d Average crystallite sizes are determined by the broadening of the CdS (002) and VC (200) facet diffraction peaks using the Scherrer formula.

The morphology and microstructure of the samples were characterized by transmission electron microscopy (TEM). Fig. 1b shows the TEM image of commercial VC, which reveals that the VC is the aggregated sheet-like particles with a size in the range of 100–500 nm. As displayed in its high-resolution TEM (HRTEM) image (inset in Fig. 1b), the VC has a well-resolved interplanar spacing of ~0.34 nm, corresponding to the in-plane (220) facets of cubic VC [39], consistent with its XRD result. The TEM image shown in Fig. 1c indicates that the pristine CdS is composed of slightly aggregated nanoparticles with a diameter of 20~30 nm. The interplanar spacing of the two lattice fringes on the CdS nanoparticles is about is ~0.16 nm (inset in Fig. 1c), corresponding to the (101) plane of the hexagonal phase CdS nanoparticles [3]. After integrating CdS nanoparticles with VC, the TEM image (Fig. 1d) of the resultant CdS/VC (15 wt.%) reveals that a large number of CdS nanoparticles are intimately integrated with the large-size VC particles and the CdS nanoparticles tend to aggregate into large particles. Also, it can be observed that the incorporation of VC has no significant effect on the morphology and size of CdS nanoparticles. The inset in Fig. 1d shows the SAED pattern of the CdS/VC (15 wt.%) during TEM analysis, revealing an alternate lattice spacings of CdS and VC, which further confirms the integration of CdS with VC [5]. The HRTEM image of the CdS/VC (15 wt.%) photocatalyst in Fig. 1e further indicates that the CdS nanoparticles are strongly coupled to the surfaces of sheet-like VC particles. Fig. 1f and g show the high angle annular dark field-scanning transmission electron microscopy (HAADF-STEM) image of the CdS/VC (15 wt.%) and corresponding energy dispersive X-ray (EDX) element mappings, respectively, in which the signals of Cd, S, V, and C elements are all clearly observed and uniformly distributed throughout the sample, again confirming the strong integration of CdS and VC to form a CdS/VC composite photocatalyst [10]. From above results, although the VC has a large size, its sheet-like feature is beneficial to provide large contact area for the loading of small-size CdS nanoparticles, which would be expected to offer a fast electron transport kinetics for photocatalytic HER [44].

The surface chemical states of pristine CdS, commercial VC, and CdS/VC (15 wt.%) composite photocatalyst were analyzed with the X-ray photoelectron spectroscopy (XPS). The XPS survey spectra in Fig. S4 shows the coexistence of Cd, S, V, and C elements in CdS/VC (15 wt.%), indicating the success integration of VC and CdS [9], consistent with the results of XRD and TEM measurements. Fig. 2a and b show the high-resolution XPS spectra of the Cd 3d and S 2p for the CdS and CdS/VC (15 wt.%), respectively. Compared with pristine CdS, both Cd 3d and S 2p peaks for the CdS/VC (15 wt.%) photocatalyst are shifted to the low binding energy side by ~0.8 to 0.9 eV, which is mainly originated from the strong electronic coupling between CdS and VC due to the electron transfer from VC to CdS [3]. The increase in electron density will lead to the production of more photogenerated electrons that can efficiently

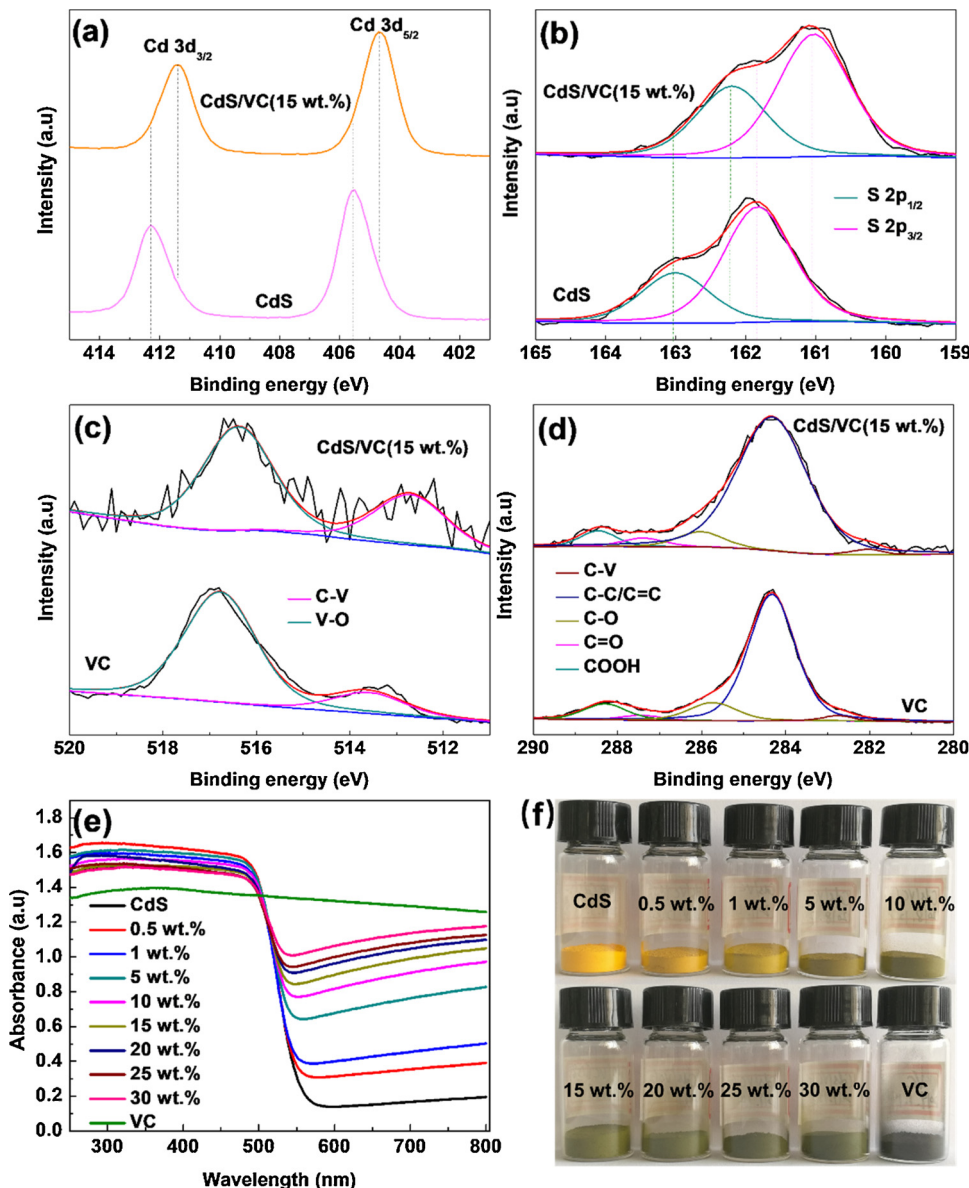
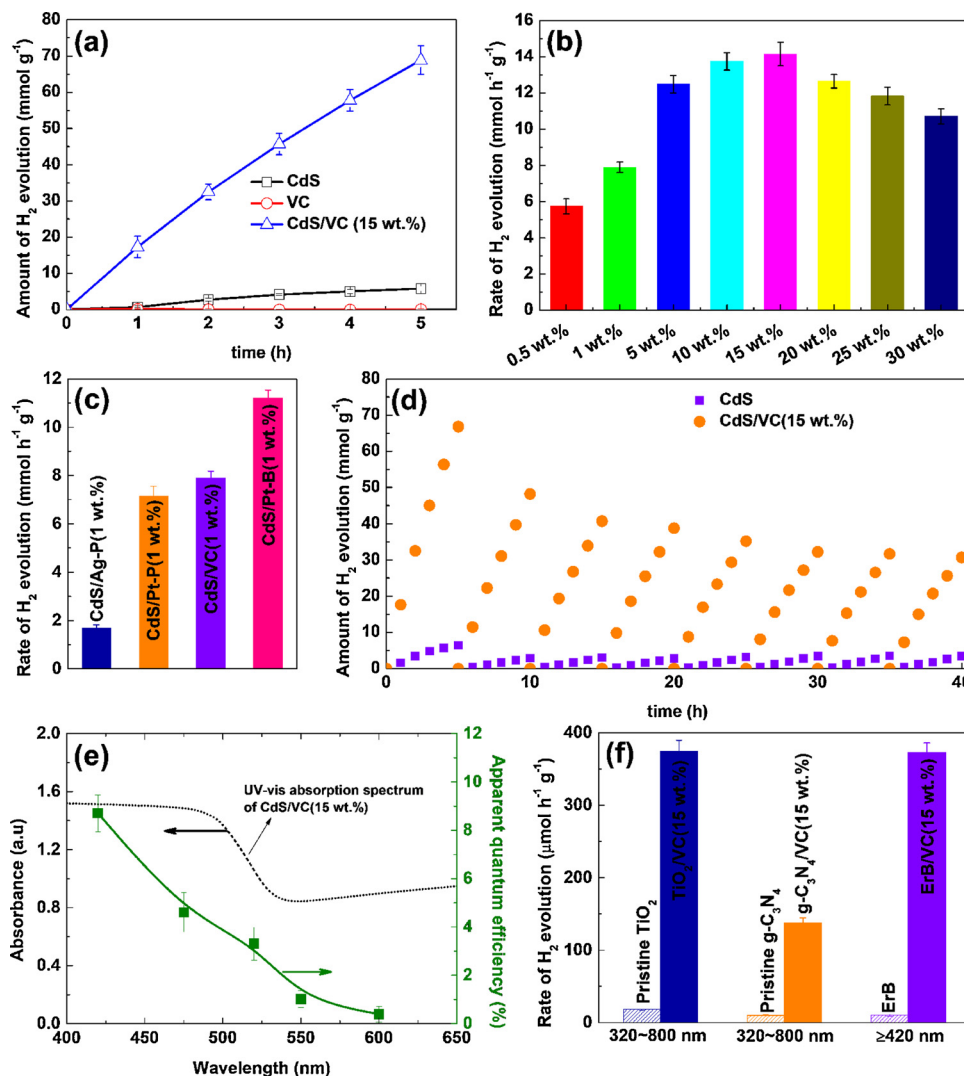


Fig. 2. (a) Cd 3d and (b) S 2p XPS spectra of pristine CdS and CdS/VC (15 wt.%). (c) V 2p and (d) C 1s XPS spectra of commercial VC and CdS/VC (15 wt.%). (e) UV-vis diffusion reflectance spectra (UV-vis DRS) of pristine CdS, commercial VC, and CdS/VC samples with different contents of VC. (f) The digital photos of the samples.

participate in the HER over CdS/VC (15 wt.%) photocatalyst under visible light irradiation. In addition, the fitting of the V 2p spectrum of the commercial VC reveals that there are two main peaks located at 513.6 and 516.8 eV, which can be attributed to the C-V and V-O species, respectively [45] (Fig. 2c). The presence of V-O species is due to the surface oxidation of VC when exposed in air since no oxides could be observed in its XRD pattern [39]. Compared to the VC, the C-V and V-O species for the CdS/VC (15 wt.%) photocatalyst occur at the lower binding energies of 512.7 and 516.4 eV, which probably due to the strong interaction between CdS and VC [3]. Moreover, the C 1s XPS spectrum (Fig. 2d) of the commercial VC can be fitted into a small peak at 282.8 eV and a number of peaks at 284.3, 285.7, 287.4, and 288.3 eV, which can be ascribed to the C-V bonds and C species (C-C/C=C, C-O, C=O, and COOH) from C contamination [43], respectively. From the C 1s XPS spectrum of the CdS/VC (15 wt.%) photocatalyst, C-V (282.0 eV) and other C species (284.3, 286.0, 287.4, and 288.5 eV) could also be observed but with lower binding energies compared to that of the VC, further indicating the strong integration of CdS with VC.

Fig. 2e shows the UV-vis diffusion reflectance spectra (UV-vis-DRS)

of the pristine CdS, commercial VC, and CdS/VC composite photocatalysts along with their colors (Fig. 2f). It can be seen that pristine CdS exhibits a strong light absorption from 300 to 500 nm with a sharp edge of 560 nm (corresponding to a band gap of 2.2 eV), while the commercial VC shows an intense absorption from 300 to 800 nm, indicating its metallic nature [45]. Notably, all the CdS/VC photocatalysts show similar intrinsic band gap absorption to pristine CdS nanoparticles, which indicates that the integration of VC has no effect on the intrinsic optical properties of the CdS [5,12], and the CdS nanoparticles may exist on the surface of the sheet-like VC particles. Moreover, with increasing VC content in CdS/VC composite photocatalysts, a gradually enhanced absorption from 560 to 800 nm accompanied with an obvious color change from yellow to black green can be observed due to the black color of VC (Fig. 2f). Furthermore, no obvious shift in the absorption edge of CdS/VC photocatalysts is observed, indicating that V or C element is not doped into the crystal structure of CdS [4], which is in good agreement with the XRD data. These results indicate that the integration of VC with CdS nanoparticles will lead to enhanced light harvesting ability for the resultant CdS/VC



photocatalysts, which will render the formation of more photo-generated electrons upon light irradiation, thus improving the photocatalytic activity for HER [25,46].

The photocatalytic HER activity of the samples was evaluated under visible light irradiation using 10 vol.% LA as the sacrificial reagent. Fig. 3a shows the time courses of photocatalytic H₂ evolution of the pristine CdS, commercial VC, and CdS/VC (15 wt.%) photocatalyst. Despite high absorption ability toward visible light, the H₂ evolution activity of CdS is quite low (1.19 mmol h⁻¹ g⁻¹) probably due to the rapid recombination of photogenerated charge carriers [14–18], while the VC alone shows no activity for HER because of the lack of a band gap for generating photoelectrons. Notably, after integrating VC with CdS, the resultant CdS/VC (15 wt.%) photocatalyst demonstrates an exceptionally high photocatalytic H₂ evolution activity. The rate of photocatalytic H₂ evolution on CdS/VC (15 wt.%) photocatalyst is as high as 14.2 mmol h⁻¹ g⁻¹, which is much higher than that of pristine CdS. Fig. 3b shows the average rate of H₂ evolution for CdS/VC photocatalysts with different contents of VC. Compared to the pristine CdS, after integrating a very small amount of VC (0.5 wt.%) with CdS, the H₂ evolution rate of the obtained CdS/VC (0.5 wt.%) is enhanced to 5.74 mmol h⁻¹ g⁻¹. With the further increase in VC content, the H₂ evolution rate of CdS/VC photocatalysts enhances considerably and maximizes at a VC content of 15 wt.% (CdS/VC (15 wt.%)), which exhibits the highest H₂ evaluation rate of 14.2 mmol h⁻¹ g⁻¹, up to 12 times higher than that of pristine CdS. The catalytic H₂ evolution activity of VC is also comparable to or even higher than that of most

recently reported noble-metal-free cocatalysts in semiconductor-based photocatalytic H₂ evolution systems (Table S1). Further increasing VC content will lead to a slight decrease in H₂ evolution activity probably due to the severe light shield effect at higher VC content [16,17]. In order to exclude the possibility that the surface VO_x species on VC particles may act as the active sites for photocatalytic HER, V₂O₅ and air-annealed VC (a-VC) (see their XRD pattern in Fig S5a) were also integrated with CdS, and the photocatalytic activities of the resultant CdS/V₂O₅ (15 wt.%) and CdS/a-VC (15 wt.%) (see their XRD patterns in Fig. S5b) were also tested. It is found that CdS/V₂O₅ exhibits comparable activity to pristine CdS, indicating that V₂O₅ is not active in catalyzing photocatalytic H₂ evolution over CdS (Fig. S5c). On the other hand, a-VC annealed at 300 °C shows much inferior activity to pristine VC due to the increased content of VO_x on the surface of VC. Increasing annealing temperature of VC to 500 °C further decreases the photocatalytic HER activity of the resultant CdS/a-VC due to the almost conversion of VC to V₂O₅. These results clearly demonstrate that the surface VO_x species on VC particles cannot act as the active sites for photocatalytic H₂ evolution and the observed good activity is mainly attributed to VC itself. In addition, the photocatalytic H₂ evolution activity of VC as a cocatalyst was compared with the commonly used noble metals such as Pt and Ag (Fig. 3c). 1 wt.% of these cocatalysts was, respectively, loaded on CdS with the in situ photoreduction method from the corresponding complexes of metals. It is worth to note that CdS/VC (1 wt.%) photocatalyst even exhibits a higher H₂ evaluation activity than 1 wt.% Pt loaded CdS photocatalyst (denoted as CdS/

Pt-P (1 wt.%) prepared by in situ photoreduction method. In light of the weaker reducing ability of photoreduction, the Pt precursor (H_2PtCl_6) might not be completely reduced to metallic Pt⁰ and loaded on the surfaces of CdS nanoparticles [41,47,48], thus resulting in a low activity. Alternatively, we also prepared CdS/Pt (1 wt.%) photocatalyst by chemical reduction method using NaBH_4 as reductant (denoted as CdS/Pt-B (1 wt.%) [41]. As displayed in Fig. 3c, the rate of H_2 evolution on CdS/Pt-B (1 wt.%) is largely enhanced but only slightly higher than that of CdS/VC (1 wt.%). These results indicate that VC would be expected to be a promising highly active cocatalyst to replace noble metals for large-scale photocatalytic H_2 evolution [39]. Considering that the VC cocatalyst used in this study has large size and low surface area, it could be expected that its catalytic activity for HER would be significantly improved by regulating its size and dispersion on the surfaces of CdS nanoparticles. Moreover, the photocatalytic H_2 evolution stability of CdS/VC (15 wt.%) was evaluated by carrying out a 40 h reaction with an intermittent evacuation every 5 h, including that of CdS for comparison. As shown in Fig. 3d, although the photocatalytic H_2 evolution activity of CdS/VC (15 wt.%) photocatalyst slowly decreases with reaction run, its activity still higher than that of the CdS at each reaction run. The used CdS/VC (15 wt.%) after a 40 h reaction was subjected to XRD analysis, as shown in Fig. S6, where no obvious changes for crystalline structure could be observed as compared to fresh CdS/VC (15 wt.%) photocatalyst. Therefore, it could be inferred that the decrease in activity for CdS/VC (15 wt.%) is probably due to the photocorrosion of CdS [6,13], while the VC is relatively stable. Fig. 3e presents the apparent quantum efficiency (AQE) of H_2 evolution on CdS/VC (15 wt.%) photocatalyst under the light irradiation of different wavelengths. The highest AQE of H_2 evolution is determined to be 8.7% under the light irradiation of 420 nm. With the increase in wavelength of the incident light, the AQE of H_2 evolution on CdS/VC (15 wt.%) gradually decreases and deviates from its light absorption spectrum especially at longer wavelengths. This result clearly indicates that the light absorption property of CdS dominates the HER and the excess light absorption originated from VC has no contribution to the observed activity, suggesting that the VC mainly act as a cocatalyst instead of a photosensitizer in CdS/VC (15 wt.%) composite photocatalyst [43]. To verify that the VC can act as a versatile and active HER cocatalyst on different semiconductor photocatalysts, we integrated VC with TiO_2 and $\text{g-C}_3\text{N}_4$, respectively, and tested the photocatalytic H_2 evolution activity of the resultant photocatalysts. As shown in Fig. 3f, a simple integration of TiO_2 and $\text{g-C}_3\text{N}_4$ with 15 wt.% VC increase the photocatalytic H_2 evolution activities of the resultant TiO_2/VC (15 wt.%) and $\text{g-C}_3\text{N}_4/\text{VC}$ (15 wt.%) composite photocatalysts by factors of 20 and 13.8, respectively, as compared with that of pristine TiO_2 and $\text{g-C}_3\text{N}_4$. In addition, VC also shows a high activity in catalyzing photochemical H_2 evolution in an Erythrosin B-triethanolamine (ErB-TEOA) system under visible light irradiation. These findings clearly show the great potential of VC as a versatile HEC that can be coupled with various semiconductor photocatalysts and dye-sensitized systems for efficient conversion of solar energy into H_2 energy [39,45].

The effect of different electron donors on the photocatalytic activity of CdS/VC (15 wt.%) composite photocatalyst was investigated by varying the electron donors from basic TEOA (10 vol.%, pH 11.3) and $\text{Na}_2\text{S-Na}_2\text{SO}_3$ (0.5 M, pH 14.0) to nearly neutral ethanol (10 vol.%, pH 5.6), and to acidic acetic acid (0.1 M, pH 2.0) and LA (10 vol.%, pH 1.2). As shown in Fig. S7, the photocatalytic activity of the CdS/VC (15 wt.%) photocatalyst in the presence of LA is the highest among the electron donors tested due to the strong acidic conditions [4]. In addition, the LA has a smaller oxidation potential (1.34 V versus normal hydrogen electrode (NHE) than acetic acid (1.58 V vs. NHE) [10], thus the highest H_2 evolution rate was obtained when LA was used as electron donor, as LA is most easily oxidized. On the other hand, LA can also provide electrons to CdS, thus the oxidative degradation of VC and CdS is effectively suppressed, which will be helpful for maintaining the stability of the CdS/VC (15 wt.%) photocatalyst [19]. Moreover, the

effect of the integration process of the CdS/VC (15 wt.%) photocatalyst on the photocatalytic activity was studied (Fig. S8). It is found that the CdS/VC (15 wt.%)*-m* prepared by simply mixing CdS and VC in reaction solution shows an enhanced H_2 evolution activity compared to the pristine CdS. After the solution mixing of CdS and VC, the additional filtration and drying processes will further enhance the activity of the resultant CdS/VC (15 wt.%)*-i*, most likely due to the improved interfacial contact between two components. In order to further improve the interface properties of CdS and VC, the CdS/VC (15 wt.%)*-i* was further annealed at 100 to 400 °C for 3 h in N_2 . It can be found that the CdS/VC (15 wt.%)*-i* obtained at 100 °C only shows slightly higher activity than untreated one, and the higher annealing temperature will deteriorate the photocatalytic activity. From the XRD analysis, it is found that the crystalline structures of CdS and VC in CdS/VC (15 wt.%) composite photocatalysts remain unchanged while the particle size of CdS slightly changes (Fig S9). In order to further understand the effect of annealing on the photocatalytic activity of CdS/VC (15 wt.%), we also measured the S_{BET} of the annealed samples (Fig. S10 and Table S2). All the annealed samples showed decreased BET surface area (S_{BET}), pore size, and total pore volume as compared to unannealed one, which is probably due to the aggregations of CdS and VC. In addition, with increasing annealing temperature from 100 to 400 °C, although the S_{BET} showed no significant change, the pore size and total pore volume changed irregularly, suggesting that the dispersion and aggregation states of CdS and VC vary during the annealing processes, which will further influence the interfacial contact properties between CdS and VC. Therefore, it could be inferred that the observed decrease in activity for annealed samples at higher temperatures is most likely due to the decrease in S_{BET} and the changes of interfacial properties between CdS and VC. The facile preparation of the CdS/VC composite photocatalyst avoiding tedious procedures makes it highly promising for large-scale photocatalytic HER.

To understand the origin of the remarkable photocatalytic H_2 evolution activity of CdS/VC composite photocatalyst, three major processes involved in photocatalytic H_2 evolution, that is, light absorption, charge separation and transfer, and surface redox reactions, were thoroughly characterized and discussed. As displayed in Figs. 2e and 3e, although the integration of VC can substantially enhance the light harvesting capability of resultant CdS/VC composite photocatalyst, the intrinsic band gap of CdS hardly changed. Thus, the enhanced light absorption arising from VC unlikely accounts for the observed activity enhancement for CdS/VC composite photocatalyst [39,45]. This also suggest that the VC may play an important role in charge separation and transfer as well as surface redox reactions, which was then studied by electrocatalytic H_2 evolution experiment, transient photocurrent response measurement, electrochemical impedance spectroscopy (EIS), and steady-state and time-resolved photoluminescence (PL) spectroscopy.

Fig. 4a presents the electrocatalytic HER polarization curves of pristine CdS, commercial VC, and CdS/VC (15 wt.%) samples loaded on carbon paper (CP) in a mixed solution of 0.5 M Na_2SO_4 containing 10 vol.% LA (pH 1.2) at a scan rate of 5 mV s^{-1} . The pristine CP without loading any catalysts shows no electrocatalytic HER activity. In contrast, CP/VC electrode shows an increased cathodic HER current with the increase of the applied potential, while the CP/CdS electrode exhibits much lower catalytic HER current due to the lack of active sites for $\text{H}^+/\text{H}_2\text{O}$ reduction. After integrating VC with CdS, the catalytic HER current density is further increased for the CP/CdS/VC (15 wt.%) electrode. As shown in Fig. 1b-d, pristine sheet-like VC particles are severely aggregated, which will lead to a low HER activity due to the limited exposure of active sites. As to the CdS/VC (15 wt.%), the CdS nanoparticles (20 ~ 30 nm) will decorated on the surfaces of sheet-like VC and serve as the spacer to increase the dispersion of VC particles, resulting in an increased exposure of active sites and thus enhanced HER activity for CdS/VC (15 wt.%). In order to get kinetic insights into the enhanced electrocatalytic HER activity on the CdS/VC (15 wt.%),

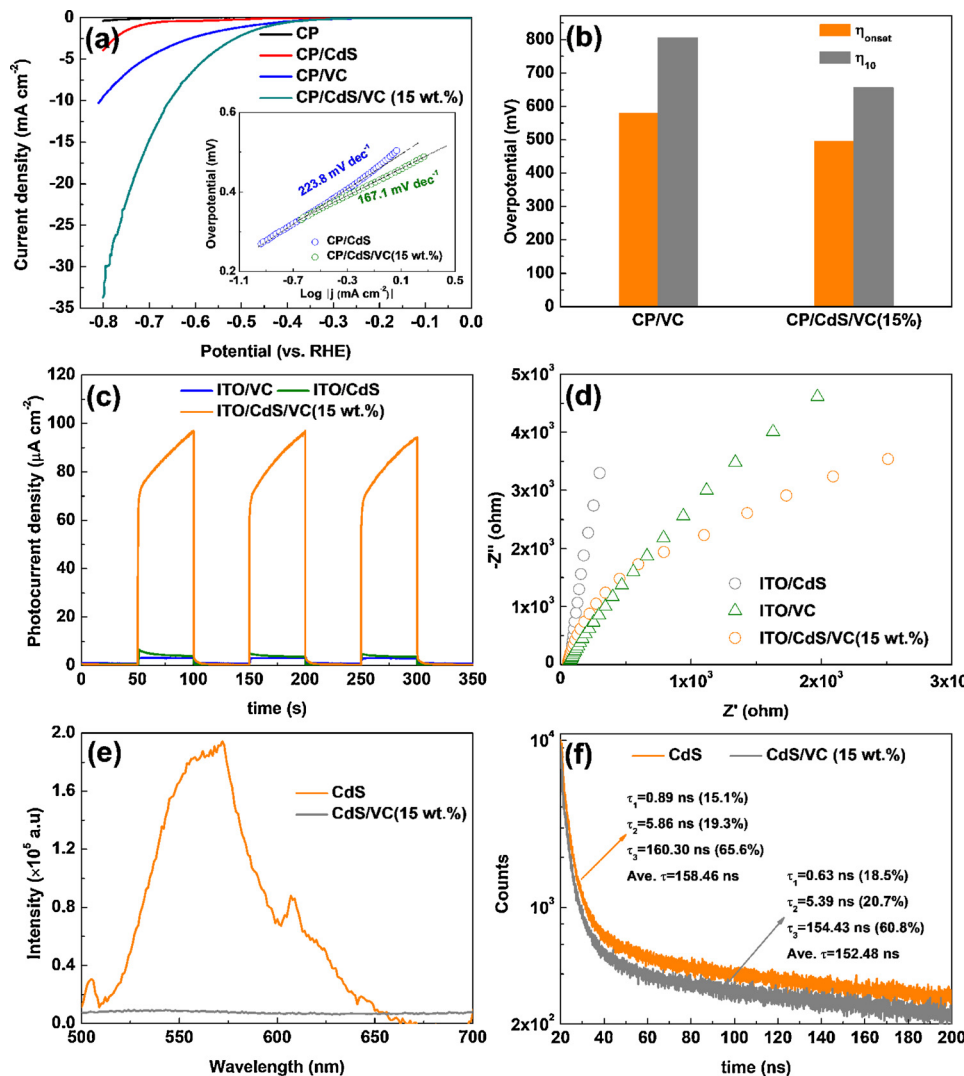


Fig. 4. (a) Electrocatalytic HER polarization curves for CP, CP/CdS, CP/VC, and CP/CdS/VC (15 wt.%) electrodes in 0.5 M Na_2SO_4 solution containing 10 vol.% LA (pH 1.2) at a scan rate of 5 mV s^{-1} . The inset shows the corresponding Tafel plots. (b) The onset potential (at a current density of 2 mA cm^{-2}) and the overpotential required to reach a current density of 10 mA cm^{-2} for CP/VC and CP/CdS/VC (15 wt.%). (c) Transient photocurrent density-time curves for ITO/CdS, ITO/VC, and ITO/CdS/VC (15 wt.%) in 0.5 M Na_2SO_4 solution containing 10 vol.% LA (pH 1.2) at a bias of 0.5 V under visible light irradiation. (d) EIS Nyquist plots of ITO/CdS, ITO/VC, and ITO/CdS/VC (15 wt.%) measured at open-circle potential under visible light irradiation in 0.5 M Na_2SO_4 solution containing 10 vol.% LA (pH 1.2). (e) Steady-state PL spectra of pristine CdS and CdS/VC (15 wt.%). Excitation wavelength: 370 nm . (f) Time-resolved PL emission decay curves of pristine CdS and CdS/VC (15 wt.%). Excitation and detection wavelengths are 370 and 550 nm , respectively.

the Tafel slopes were extracted by fitting the linear portions of the Tafel plots using the Tafel equation ($\eta = a + b \log(j/J)$, where j is the current density, b is the Tafel slope) [39]. As shown in the inset of Fig. 4a, it is clear that the CP/CdS/VC (15 wt.%) electrode exhibits a smaller Tafel slope of $167.1 \text{ mV dec}^{-1}$ than CP/VC electrode ($223.8 \text{ mV dec}^{-1}$), implying a fast HER kinetics for achieving a superior HER activity [39,45]. In addition, the onset potentials and the overpotentials required to achieve a current density of 10 mA cm^{-2} are compared in Fig. 4b and follow an order of CP/CdS/VC < CP/VC. These results confirm that VC could act as an efficient HEC to promote the surface $\text{H}^+/\text{H}_2\text{O}$ reaction when integrated with CdS under visible light irradiation.

The transient photocurrent density vs. time curves of pristine CdS, commercial VC, and CdS/VC (15 wt.%) coated on ITO were measured in a mixed solution of 0.5 M Na_2SO_4 solution containing 10 vol.% LA (pH 1.2) at a forward bias of 0.5 V under chopped visible light irradiation. As shown in Fig. 4c, the ITO/VC electrode shows negligible photocurrent response due to the lack of a band gap for the photo-electron generation, while the ITO/CdS electrode shows a relatively small photocurrent density at each on-off light irradiation owing to the rapid charge recombination [3,10]. In comparison to ITO/CdS electrode, the ITO/CdS/VC (15 wt.%) electrode shows a considerably increased photocurrent response, indicating that the integration of VC with CdS can effectively suppress the charge recombination in the resultant CdS/VC (15 wt.%) photocatalyst [10,43]. The origin of the

enhanced charge separation efficiency is further studied by EIS measurement. As depicted in Fig. 4d, ITO/CdS/VC (15 wt.%) exhibits a much smaller semicircle diameter than ITO/VC and ITO/CdS, suggesting an obviously reduced charge transfer resistance at the interface between CdS and VC [4,10], which is favorable to enhance the charge separation efficiency of the CdS/VC (15 wt.%) photocatalyst. Furthermore, due to the recombination of electron-hole pair in semiconductors gives rise to photoluminescence (PL), the monitoring of which allows us to study the efficiency of charge carrier separation in semiconductor photocatalysts [49–51]. In this case, compared with pristine CdS, the integration of VC with CdS might lead to the formation of Schottky junctions due to the metallic properties of VC, which are expected to strongly enhance the separation efficiency of photogenerated carriers. Fig. 4e shows steady-state PL spectra of the pristine CdS and CdS/VC (15 wt.%) photocatalyst, and the PL spectra of the CdS/VC photocatalysts with different contents of VC were given in Fig. S11. Pristine CdS shows a strong and broad emission band centered at 560 nm , which can be attributed to the radiative recombination of electron-hole pairs in CdS. On the contrary, the PL emissions of all the CdS/VC composite photocatalysts is remarkably quenched due to the presence of VC, and the quenching efficiency increases with increasing VC content, suggesting a low recombination rate of photogenerated charge carriers. This is most likely attributed to the effective charge transfer from the conduction band edge of pristine CdS to the Fermi level of VC [49–51]. In order to confirm the quenching of PL emission for the CdS/VC

(15 wt.%) photocatalyst is through the electron transfer from CdS to VC, the decay profiles of PL emission at 550 nm were acquired (Fig. S12) by time-resolved PL (TRPL) measurements. The lifetimes were obtained by fitting TRPL curves with a triexponential decay function to optimize the fitting accuracy. As shown in Fig. 4f, for the TPRL curve of the pristine CdS, the fitting result shows one short-lived component and two long-lived components with lifetimes of 0.89 (15.1%) (τ_1), 5.86 (19.3%) (τ_2) and 160.30 ns (65.6%) (τ_3), respectively, and the intensity-averaged PL lifetime ($<\tau>$) is calculated to be 158.46 ns. In comparison to pristine CdS, CdS/VC (15 wt.%) shows a reduced short (τ_1 : 0.63 ns), long (τ_2 : 5.39 ns, τ_3 : 154.43 ns), and intensity-averaged lifetimes ($<\tau>$: 152.48 ns). Thus, consistent with the observations in the literatures [52–58], it can be inferred that dynamic electron transfer from photoexcited CdS to VC is the dominant pathway for quenching the PL emission of the CdS/VC (15 wt.%), whereas the PL quenching for the pristine CdS has been only due to the band edge recombination [10,43]. All above photoelectrochemical and PL results suggest that the integration of VC can greatly suppress the recombination of photo-generated charge carriers, presumably by providing rapid electron transfer pathway and accepting photoexcited electrons in CdS, which will in turn significantly improve the photocatalytic H₂ evolution activity of CdS/VC (15 wt.%) photocatalyst [13,14,17,52,54,56].

On the basis of above experimental results, a plausible photocatalytic mechanism is proposed to explain the high photocatalytic H₂ evolution activity of CdS/VC composite photocatalyst under visible light irradiation, as shown in Fig. 5. Upon visible light irradiation, the CdS in CdS/VC composite photocatalyst can be excited to produce electrons (e⁻) and holes (h⁺). Thanks to the outstanding metallic properties of VC [39,45], the photogenerated electrons in the CB of CdS can rapidly transfer to VC, leaving the holes in the valence band (VB) of CdS, and thus leading to an efficient separation of photogenerated carriers. At the same time, similar to the noble metals and other TMCs loaded CdS photocatalysts [14–18], the accumulation of the negative charges in VC and the positive charges in CdS near the contact interface of CdS and VC will lead to the formation of a space charge layer, and thus the CB and VB of CdS are bent “upward”, as a result, a Schottky junction is formed between CdS and VC [20–23]. Hence, when the photogenerated electrons in the CB of CdS migrate across the interface to VC, the Schottky junction can act as an electron sink to efficiently capture the photogenerated electrons to greatly enhance the charge transfer and separation efficiency for CdS/VC composite photocatalyst, as shown in Fig. 4c–f. On the other hand, after photogenerated electrons being transferred to the surface active sites on VC, the protons in the aqueous solution are efficiently reduced to form H₂ gas due to the outstanding catalytic HER activity of VC (Fig. 4a and b). In contrast, owing to the rapid recombination of photogenerated carriers as well as

the lack of surface active sites for HER, the pristine CdS photocatalyst exhibits a low photocatalytic activity toward H₂ evolution [17,21,23,59].

4. Conclusions

In summary, we have identified that VC can function as an efficient cocatalyst to significantly enhance the photocatalytic H₂ evolution activity of visible-light-responsive CdS nanoparticles under visible light irradiation (≥ 420 nm). The VC could be integrated with CdS with a simple solution-based mixing method, greatly simplifying the activity optimization of the resultant CdS/VC composites photocatalyst for practical application. The most efficient CdS/VC (15 wt.%) photocatalyst shows 12 times higher activity toward H₂ evolution than pristine CdS nanoparticles. In addition, CdS/VC (15 wt.%) photocatalyst shows a relatively stable HER activity. Moreover, the AQE of photocatalytic H₂ evolution reaches up to 8.7% at 420 nm. More significantly, the catalytic HER activity of VC is much higher than that of Ag and comparable to that of Pt over CdS. According to the electrochemical and photoelectrochemical results, it is found that VC can act as an efficient electrocatalyst to reduce the overpotential of H⁺/H₂O reduction to H₂. On the other hand, VC can also effectively capture and transfer the photogenerated electrons of CdS to enhance the separation efficiency of photogenerated carriers due to its metallic nature, thus substantially improving the photocatalytic activity of CdS/VC composite photocatalysts. In addition, the versatility of VC as an efficient cocatalyst is also confirmed with various semiconductor photocatalysts and dye-sensitized system. Therefore, the superior catalytic activity of VC on CdS excitingly confirms the feasibility of the V-based materials as potential substitutes to noble metals for designing highly efficient, stable, and cost-effective semiconductor photocatalysts and dye-sensitized systems for photocatalytic H₂ evolution from water splitting.

Acknowledgements

This work is supported by the National Natural Science Foundation of China (Grant No. 21763001 and 21463001), the Natural Science Foundation of Ningxia Province (Grant No. 2018AAC02011), the West Light Foundation of the Chinese Academy of Sciences (Grant No. XAB2018AW13), the Research Program of Science and Technology at Universities of Ningxia Province (Grant No. NGY2018-156), the Fundamental Research Funds for the Central Universities, North Minzu University (2019XYZHG02), the Foundation of Key Laboratory of Electrochemical Energy Conversion Technology and Application, the Foundation of Training Program for Yong and Middle-aged Talents of State Ethnic Affairs Commission of China, and the Graduate student

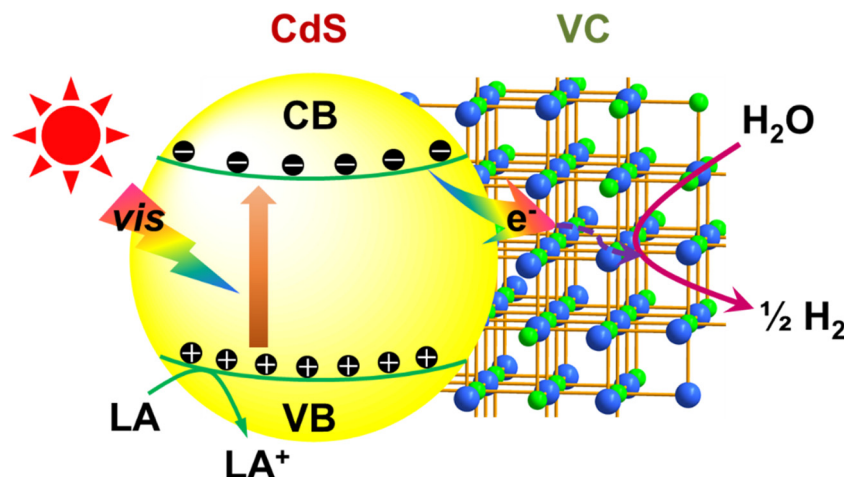


Fig. 5. Plausible photocatalytic mechanism for H₂ evolution on CdS/VC photocatalyst under visible light irradiation.

innovation project at North Minzu University (YCX18078 and YCX19119).

Appendix A. Supplementary data

Supplementary material related to this article can be found, in the online version, at doi:<https://doi.org/10.1016/j.apcatb.2019.118029>.

References

- X. Chen, S. Shen, L. Guo, S. Mao, Semiconductor-based photocatalytic hydrogen generation, *Chem. Rev.* 110 (2010), <https://doi.org/10.1021/cr0016456503>.
- X. Yue, S. Yi, R. Wang, Z. Zhang, S. Qiu, Well-controlled $\text{SrTiO}_3@\text{Mo}_2\text{C}$ core-shell nanofiber photocatalyst: Boosted photo-generated charge carriers transportation and enhanced catalytic performance for water reduction, *Nano Energy* 47 (2018) 463–473, <https://doi.org/10.1016/j.nanoen.2018.03.014>.
- A. Wu, C. Tian, Y. Jiao, Q. Yan, G. Yang, H. Fu, Sequential two-step hydrothermal growth of MoS_2/CdS core-shell heterojunctions for efficient visible light-driven photocatalytic H_2 evolution, *Appl. Catal. B: Environ.* 203 (2017) 955–963, <https://doi.org/10.1016/j.apcatb.2016.11.009>.
- S. Min, Y. Lei, H. Sun, J. Hou, F. Wang, E. Cui, S. She, Z. Jin, J. Xu, X. Ma, Amorphous WS_x as an efficient cocatalyst grown on CdS nanoparticles via photochemical deposition for enhanced visible-light-driven hydrogen evolution, *Mol. Catal.* 440 (2017) 190–198, <https://doi.org/10.1016/j.mcat.2017.07.023>.
- Q. Li, B.D. Guo, J.G. Yu, J.R. Ran, B.H. Zhang, H.J. Yan, J.R. Gong, Highly efficient visible-light-driven photocatalytic hydrogen production of CdS -cluster-decorated graphene nanosheets, *J. Am. Chem. Soc.* 133 (2011) 10878–10884, <https://doi.org/10.1021/ja2025454>.
- H. Li, Z.B. Xia, J.Q. Chen, L. Lei, J.H. Xing, Constructing ternary CdS /reduced graphene oxide/ TiO_2 nanotube arrays hybrids for enhanced visible-light-driven photoelectrochemical and photocatalytic activity, *Appl. Catal. B: Environ.* 168–169 (2015) 105–113, <https://doi.org/10.1016/j.apcatb.2014.12.029>.
- W. Zhang, X. Chen, J. Zhang, C. Tuo, L. Ji, H. Li, X. Zhang, F. Yang, Exposure of active edge structure for electrochemical H_2 evolution from $\text{VS}_2/\text{MWCNTs}$ hybrid catalysts, *Int. J. Hydrogen Energy* 43 (2018) 22949–22954, <https://doi.org/10.1016/j.ijhydene.2018.10.168>.
- Y. Xue, Y. Lei, X. Liu, Y. Li, W. Deng, F. Wang, S. Min, Highly active dye-sensitized photocatalytic H_2 evolution catalyzed by a single-atom Pt cocatalyst anchored onto $\text{g-C}_3\text{N}_4$ nanosheets under long-wavelength visible light irradiation, *New J. Chem.* 42 (2018) 14083–14086, <https://doi.org/10.1039/C8NJ02933D>.
- J. Hou, Y. Lei, F. Wang, X. Ma, S. Min, Z. Jin, J. Xu, In-situ photochemical fabrication of transition metal-promoted amorphous molybdenum sulfide catalysts for enhanced photosensitized hydrogen evolution, *Int. J. Hydrogen Energy* 42 (2017) 11118–11129, <https://doi.org/10.1016/j.ijhydene.2017.01.235>.
- Y. Lei, J. Hou, F. Wang, X. Ma, Z. Jin, J. Xu, S. Min, Boosting the catalytic performance of MoS_x cocatalysts over CdS nanoparticles for photocatalytic H_2 evolution by Co doping via a facile photochemical route, *Appl. Surf. Sci.* 420 (2017) 456–464, <https://doi.org/10.1016/j.apsusc.2017.05.165>.
- P. Praus, L. Svoboda, R. Dvorský, M. Reli, M. Kormunda, P. Mančík, Ceram. Synthesis and properties of nanocomposites of WO_3 and exfoliated $\text{g-C}_3\text{N}_4$, *Ceram. Int.* 43 (2017) 13581–13591, <https://doi.org/10.1016/j.ceramint.2017.07.067>.
- K. Chang, Z. Mei, T. Wang, Q. Kang, S. Ouyang, J. Ye, $\text{MoS}_2/\text{Graphene}$ cocatalyst for efficient photocatalytic H_2 evolution under visible light irradiation, *ACS Nano* 8 (2014) 7078–7087, <https://doi.org/10.1021/nn5019945>.
- G. Yu, L. Geng, S. Wu, W. Yan, G. Liu, Highly-efficient cocatalyst-free H_2 -evolution over silica-supported CdS nanoparticle photocatalysts under visible light, *Chem. Commun.* 51 (2015) 10676–10679, <https://doi.org/10.1039/C5CC02249E>.
- L. Huang, X. Wang, J. Yang, G. Liu, J. Han, C. Li, Dual cocatalysts loaded type I CdS/ZnS core/shell nanocrystals as effective and stable photocatalysts for H_2 evolution, *J. Phys. Chem. C* 117 (2013) 11584–11591, <https://doi.org/10.1021/jp400010z>.
- X. Yin, J. Liu, W. Jiang, X. Zhang, J. Hu, L. Wan, Urchin-like $\text{Au}@\text{CdS}/\text{WO}_3$ micro/nano heterostructure as a visible-light driven photocatalyst for efficient hydrogen generation, *Chem. Commun.* 51 (2015) 13842–13845, <https://doi.org/10.1039/C5CC05211D>.
- Z. Fang, Y. Wang, J. Song, Y. Sun, J. Zhou, R. Xu, H. Duan, Immobilizing CdS quantum dots and dendritic Pt nanocrystals on thiolated graphene nanosheets toward highly efficient photocatalytic H_2 evolution, *Nanoscale* 5 (2013) 9830–9838, <https://doi.org/10.1039/C3NR03043A>.
- D. Ma, J. Shi, Y. Zou, Z. Fan, X. Ji, C. Niu, L. Wang, Rational design of CdS/ZnO core-shell structure via atomic layer deposition for drastically enhanced photocatalytic H_2 evolution with excellent photostability, *Nano Energy* 39 (2017) 183–191, <https://doi.org/10.1016/j.nanoen.2017.11.048>.
- S. Tso, W. Li, B. Wu, L. Chen, Enhanced H_2 production in water splitting with CdS/ZnO core-shell nanowires, *Nano Energy* 43 (2018) 270–277, <https://doi.org/10.1016/j.nanoen.2017.11.048>.
- Q. Li, B. Guo, J. Yu, J. Ran, B. Zhang, H. Yan, J.R. Gong, Highly efficient visible-light-driven photocatalytic hydrogen production of CdS -cluster-decorated graphene nanosheets, *J. Am. Chem. Soc.* 133 (2011) 10878–10884, <https://doi.org/10.1021/ja2025454>.
- H. Li, X. Yan, B. Lin, M. Xia, J. Wei, B. Yang, G. Yang, Controllable spatial effect acting on photo-induced $\text{CdS}@\text{CoP}@/\text{SiO}_2$ ball-in-ball nano-photoreactor for enhancing hydrogen evolution, *Nano Energy* 47 (2018) 481–493, <https://doi.org/10.1016/j.nanoen.2018.03.026>.
- H. Zhao, Z. Hu, J. Liu, Y. Li, M. Wu, G. Tendeloo, B. Su, Blue-edge slow photons promoting visible-light hydrogen production on gradient ternary 3DOM $\text{TiO}_2\text{-Au-CdS}$ photonic crystals, *Nano Energy* 47 (2018) 266–274, <https://doi.org/10.1016/j.nanoen.2018.02.052>.
- X. Yin, G. He, B. Sun, W. Jiang, D. Xue, A. Xia, L. Wan, J. Hu, Rational design and electron transfer kinetics of MoS_2/CdS nanodots-on-nanorods for efficient visible-light-driven hydrogen generation, *Nano Energy* 28 (2016) 319–329, <https://doi.org/10.1016/j.nanoen.2016.08.037>.
- Y. Liu, S. Ding, Y. Shi, X. Liu, Z. Wu, Q. Jiang, T. Zhou, N. Liu, J. Hu, Construction of CdS/CoO_x core-shell nanorods for efficient photocatalytic H_2 evolution, *Appl. Catal. B: Environ.* 234 (2018) 109–116, <https://doi.org/10.1016/j.apcatb.2018.04.037>.
- K. Zhang, S. Qian, W.J. Kim, J.K. Kim, X. Sheng, J.Y. Lee, J.H. Park, Double 2-Dimensional H_2 -evolving catalyst tipped photocatalyst nanowires: a new avenue for high-efficiency solar to H_2 generation, *Nano Energy* 34 (2017) 481–490, <https://doi.org/10.1016/j.nanoen.2017.03.005>.
- Y. Sui, S. Liu, T. Li, Q. Liu, T. Jiang, Y. Guo, J. Luo, Atomically dispersed Pt on specific TiO_2 facets for photocatalytic H_2 evolution, *J. Catal.* 353 (2017) 250–255, <https://doi.org/10.1016/j.jcat.2017.07.024>.
- B. Cao, G. Li, H. Li, Hollow spherical $\text{RuO}_2@\text{TiO}_2@\text{Pt}$ bifunctional photocatalyst for coupled H_2 production and pollutant degradation, *Appl. Catal. B: Environ.* 194 (2016) 42–49, <https://doi.org/10.1016/j.apcatb.2016.04.033>.
- Y. Kuo, C.D. Frye, M. Ikenberry, K.J. Klabunde, Titanium-indium oxy (nitride) with and without RuO_2 loading as photocatalysts for hydrogen production under visible light from water, *Catal. Today* 199 (2013) 15–21, <https://doi.org/10.1016/j.cattod.2012.03.012>.
- W. Chen, Y. Wang, W. Shangguan, Metal (oxide) modified ($\text{M} = \text{Pd, Ag, Au and Cu}$) $\text{H}_2\text{SrTa}_2\text{O}_7$ for photocatalytic CO_2 reduction with H_2O : the effect of cocatalysts on promoting activity toward CO and H_2 evolution, *Int. J. Hydrogen Energy* 44 (2019) 4123–4132, <https://doi.org/10.1016/j.ijhydene.2018.12.166>.
- Y. Xie, Y. Zheng, Y. Yang, R. Jiang, G. Wang, Y. Zhang, E. Zhang, L. Zhao, C. Duan, Two-dimensional nickel hydroxide/sulfides nanosheet as an efficient cocatalyst for photocatalytic H_2 evolution over CdS nanospheres, *J. Colloid Interface Sci.* 514 (2018) 634–641, <https://doi.org/10.1016/j.jcis.2017.12.080>.
- O. Carrasco-Jaím, R. Ahumada-Lazo, P. Clark, Photocatalytic hydrogen production by biomimetic indium sulfide using *Mimosa pudica* leaves as template, *Int. J. Hydrogen Energy* 44 (2019) 2770–2783, <https://doi.org/10.1016/j.ijhydene.2018.12.043>.
- M. Liu, B. Chen, R. Li, C. Li, H. Zou, C. Huang, Dendritic CuSe with hierarchical side-branches: synthesis, efficient adsorption, and enhanced photocatalytic activities under daylight, *ACS Sustainable Chem. Eng.* 5 (2017) 4154–5160, <https://doi.org/10.1021/acssuschemeng.7b00126>.
- R. Godin, Y. Wang, M.A. Zwijsenborg, J. Tang, J.R. Durrant, Time-resolved spectroscopic investigation of charge trapping in carbon nitrides photocatalysts for hydrogen generation, *J. Am. Chem. Soc.* 139 (2017) 5216–5224, <https://doi.org/10.1021/jacs.7b01547>.
- Y. Zou, D. Ma, D. Sun, S. Mao, C. He, Z. Wang, X. Ji, J. Shi, Carbon nanosheet facilitated charge separation and transfer between molybdenum carbide and graphitic carbon nitride toward efficient photocatalytic H_2 production, *Appl. Surf. Sci.* 475 (2019) 91–101, <https://doi.org/10.1016/j.apsusc.2018.12.102>.
- S. Meyer, A.V. Nikiforov, I.M. Petrushina, K. Kohler, E. Christensen, J. Jensen, N. Bjerrum, Transition metal carbides ($\text{WC, Mo}_2\text{C, TaC, NbC}$) as potential electrocatalysts for the hydrogen evolution reaction (HER) at medium temperatures, *Int. J. Hydrogen Energy* 40 (2015) 2905–2911, <https://doi.org/10.1016/j.ijhydene.2014.12.076>.
- J. Dong, Y. Shi, C. Huang, Q. Wu, T. Zeng, W. Yao, A new and stable $\text{Mo-Mo}_2\text{C}$ modified $\text{g-C}_3\text{N}_4$ photocatalyst for efficient visible light photocatalytic H_2 production, *Appl. Catal. B: Environ.* 243 (2019) 27–35, <https://doi.org/10.1016/j.apcatb.2018.10.016>.
- J. Ran, G. Gao, F. Li, T. Ma, A. Du, S. Qiao, Ti_3C_2 MXene co-catalyst on metal sulfide photo-absorbers for enhanced visible-light photocatalytic hydrogen production, *Nat. Commun.* 8 (2017) 13907–13917, <https://doi.org/10.1038/ncomms13907>.
- S. Ma, Y. Deng, J. Xie, K. He, W. Liu, X. Chen, X. Li, Noble-metal-free Ni_3C cocatalysts decorated CdS nanosheets for high-efficiency visible-light-driven photocatalytic H_2 evolution, *Appl. Catal. B: Environ.* 227 (2018) 218–228, <https://doi.org/10.1016/j.apcatb.2018.01.031>.
- J. Zhang, M. Wu, B. He, R. Wang, H. Wang, Y. Gong, Facile synthesis of rod-like $\text{g-C}_3\text{N}_4$ by decorating Mo_2C co-catalyst for enhanced visible-light photocatalytic activity, *Appl. Surf. Sci.* 470 (2019) 565–572, <https://doi.org/10.1016/j.apsusc.2018.11.165>.
- X. Peng, L. Hu, L. Wang, X. Zhang, J. Fu, K. Huo, L. Lee, K. Wong, P. Chu, Vanadium carbide nanoparticles encapsulated in graphitic carbon network nanosheets: a high-efficiency electrocatalyst for hydrogen evolution reaction, *Nano Energy* 26 (2016) 603–609, <https://doi.org/10.1016/j.nanoen.2016.06.020>.
- H. Yan, J. Yang, G. Ma, G. Wu, X. Zong, Z. Lei, J. Shi, C. Li, Visible-light-driven hydrogen production with extremely high quantum efficiency on $\text{Pt-Pd}/\text{CdS}$ photocatalyst, *J. Catal.* 266 (2009) 165–168, <https://doi.org/10.1016/j.jcat.2009.06.024>.
- J. Jin, J. Yu, G. Liu, P.K. Wong, Single crystal CdS nanowires with high visible-light photocatalytic H_2 -production performance, *J. Mater. Chem. A* 1 (2013) 10927–10934, <https://doi.org/10.1039/c3ta12301d>.
- L. Zou, H. Wang, X. Wang, High efficient photodegradation and photocatalytic hydrogen production of CdS/BiVO_4 heterostructure through Z-scheme process, *ACS Sustainable Chem. Eng.* 5 (2017) 303–309, <https://doi.org/10.1021/acssuschemeng.6b01628>.

[43] Y. Lei, C. Yang, J. Hou, F. Wang, S. Min, X. Ma, Z. Jin, J. Xu, G. Lu, K. Huang, Strongly coupled CdS/graphene quantum dots nanohybrids for highly efficient photocatalytic hydrogen evolution: unraveling the essential roles of graphene quantum dots, *Appl. Catal. B: Environ.* 216 (2017) 59–69, <https://doi.org/10.1016/j.apcatb.2017.05.063>.

[44] X. Zong, H. Yan, G. Wu, G. Ma, F. Wen, L. Wang, C. Li, Enhancement of photocatalytic H₂ evolution on CdS by loading MoS₂ as cocatalyst under visible light irradiation, *J. Am. Chem. Soc.* 130 (2008) 7176–7177, <https://doi.org/10.1021/ja800782s>.

[45] J. Yu, X. Gao, G. Chen, X. Yuan, Electrocatalytic performance of commercial vanadium carbide for oxygen reduction reaction, *Int. J. Hydrogen Energy* 41 (2016) 4150–4158, <https://doi.org/10.1016/j.ijhydene.2016.01.008>.

[46] J. Ran, J. Zhang, J. Yu, M. Jaroniec, S.Z. Qiao, Chem. Earth-abundant cocatalysts for semiconductor-based photocatalytic water splitting, *Chem. Soc. Rev.* 43 (2014) 7787–7812, <https://doi.org/10.1039/C3CS60425J>.

[47] Y. Wang, Y. Wang, R. Xu, Photochemical deposition of Pt on CdS for H₂ evolution from water: markedly enhanced activity by controlling Pt reduction environment, *J. Phys. Chem. C* 117 (2013) 783–790, <https://doi.org/10.1021/jp309603c>.

[48] H. Huang, D.Y.C. Leung, D. Ye, Effect of reduction treatment on structural properties of TiO₂ supported Pt nanoparticles and their catalytic activity for formaldehyde oxidation, *J. Mater. Chem.* 21 (2011) 9647–9652, <https://doi.org/10.1039/C1JM10413F>.

[49] L. Spanhel, H. Weller, A. Henglein, Photochemistry of Semiconductor Colloids. 22. Electron injection from illuminated CdS into attached TiO₂ and ZnO particles, *J. Am. Chem. Soc.* 109 (1987) 6632–6635, <https://doi.org/10.1021/ja00256a012>.

[50] R. Narayanan, B.N. Reddy, M. Deepa, Facile charge propagation in CdS quantum dot cells, *J. Phys. Chem. C* 116 (2012) 7189–7199, <https://doi.org/10.1021/jp211200f>.

[51] K. Tsai, Y. Hsu, Graphene quantum dots mediated charge transfer of CdSe nanocrystals for enhancing photoelectrochemical hydrogen production, *Appl. Catal. B: Environ.* 164 (2015) 271–278, <https://doi.org/10.1016/j.apcatb.2014.09.034>.

[52] L. Shang, B. Tong, H. Yu, G. Waterhouse, C. Zhou, Y. Zhao, M. Tahir, L. Wu, C. Tung, T. Zhang, CdS nanoparticle-decorated Cd nanosheets for efficient visible light-driven photocatalytic hydrogen evolution, *Adv. Energy Mater.* 6 (2016) 1501241–1501248, <https://doi.org/10.1002/aenm.201501241>.

[53] S. Zhang, X. Liu, C. Liu, S. Luo, L. Wang, T. Cai, Y. Zeng, J. Yuan, W. Dong, Y. Pei, Y. Liu, MoS₂ quantum dot growth induced by S vacancies in a ZnIn₂S₄ monolayer: atomic-level heterostructure for photocatalytic hydrogen production, *ACS Nano* 12 (2018) 751–758, <https://doi.org/10.1021/acsnano.7b07974>.

[54] W. Liu, L. Cao, W. Cheng, Y. Cao, X. Liu, W. Zhang, X. Mou, L. Jin, X. Zheng, W. Che, Q. Liu, T. Yao, S. Wei, Single-site active cobalt-based photocatalyst with a long carrier lifetime for spontaneous overall water splitting, *Angew. Chem. Int. Ed.* 56 (2017) 9312–9317, <https://doi.org/10.1002/anie.201704358>.

[55] X. Wu, H. Zhang, J. Dong, M. Qiu, J. Kong, Y. Zhang, Y. Li, G. Xu, J. Zhang, J. Ye, Surface step decoration of isolated atom as electron pumping: atomic-level insights into visible-light hydrogen evolution, *Nano Energy* 45 (2018) 109–117, <https://doi.org/10.1016/j.nanoen.2017.12.039>.

[56] S. Cao, Y. Chen, H. Wang, J. Chen, X. Shi, H. Li, P. Cheng, X. Liu, M. Liu, L. Piao, Ultrasmall CoP nanoparticles as efficient cocatalysts for photocatalytic formic acid dehydrogenation, *Joule* 2 (2018) 549–557, <https://doi.org/10.1016/j.joule.2018.01.007>.

[57] Y. Xie, Z. Yu, G. Liu, X. Ma, H. Cheng, CdS-mesoporous ZnS core-shell particles for efficient and stable photocatalytic hydrogen evolution under visible light, *Energy Environ. Sci.* 7 (2014) 1895–1901, <https://doi.org/10.1039/c3ee43750g>.

[58] S. Iqbal, Z. Pan, K. Zhou, Enhanced photocatalytic hydrogen evolution from in situ formation of few-layered MoS₂/CdS nanosheet-based van der Waals heterostructures, *Nanoscale* 9 (2017) 6638–6642, <https://doi.org/10.1039/c7nr01705g>.

[59] T. Di, B. Cheng, W. Ho, J. Yu, H. Tang, Hierarchically CdS-Ag₂S nanocomposites for efficient photocatalytic H₂ production, *Appl. Surf. Sci.* 470 (2019) 196–204, <https://doi.org/10.1016/j.apsusc.2018.11.010>.